Chemical Science

ROYAL SOCIETY OF CHEMISTRY

EDGE ARTICLE

View Article Online
View Journal | View Issue

Cite this: *Chem. Sci.*, 2024, **15**, 1894

All publication charges for this article have been paid for by the Royal Society of Chemistry

Received 12th November 2023
Accepted 28th December 2023

DOI: 10.1039/d3sc06053e

rsc.li/chemical-science

Electronic configuration regulation of single-atomic Mn sites mediated by Mo/Mn clusters for an efficient hydrogen evolution reaction†

Chengyu Zhang,[abc] Xiangyang Wang,[abc] Renyuan Zhao,[abc] Fabrice Ndayisenga[abc] and Zhisheng Yu *[abc]

Tuning the electron distribution of metal single-atom active sites *via* bimetallic clusters is an effective way to enhance their hydrogen evolution reaction (HER) activity, but remains a great challenge. A biochar-based electrocatalyst ($BC_{MoMn800\text{-}2}$) with both MnN_4 active sites and Mo_2C/Mn_7C_3 clusters was synthesized using *in situ* enriched Mo/Mn biomass as a precursor to trigger the HER. Various characterization and density functional theory (DFT) calculation results indicated that the presence of Mo_2C/Mn_7C_3 clusters in $BC_{MoMn800\text{-}2}$ effectively induced the redistribution of charges at MnN_4 sites, reducing the energy of H* activation during the HER. In 0.5 M H_2SO_4, the overpotential was 27.4 mV at a current density of 10 mA cm^{-2} and the Tafel slope was 31 mV dec^{-1}, and its electrocatalytic performance was close to that of Pt/C. The electrocatalyst also exhibited excellent electrocatalytic stability and durability. This work might provide a new strategy for solid waste recycling and constructing efficient HER electrocatalysts.

Introduction

Excessive use of fossil fuels has caused climate change and energy crisis, which have aroused widespread concern.[1,2] To solve these problems, new renewable energy sources that are carbon-neutral are continuously being explored.[3] Hydrogen (H_2), as one of the perfect substitutes for fossil fuels, has gradually become an indispensable part of the future sustainable and clean energy system due to its excellent properties in terms of energy density, sustainability and cleanliness.[4,5] Currently, the traditional hydrogen production processes are pyrolysis of fossil fuels and reforming of natural gas.[6,7] In contrast, the production of green H_2 by water electrolysis possesses various advantages and is of great significance for global carbon neutrality.[8,9] Moreover, compared with alkaline electrolytes, water exhibits higher current densities and energy conversion efficiencies in acidic electrolytes, which could enhance the efficiency of H_2 production in large-scale industries.[10,11] However, in such an environment of acidic corrosion or strong oxidation potential, most catalysts are prone to dissolve and fall off from the electrode, resulting in a significant decrease in their catalytic activity and stability, thus limiting their practical applications.[12] Therefore, the synthesis of high-efficiency catalysts that could achieve high current density and long-term stability is of great significance for the large-scale application of water electrolysis hydrogen production technology.

Traditional noble metal catalysts, such as Pt, exhibit excellent electrocatalytic performance for the hydrogen evolution reaction (HER), but inherent defects (high cost and limited reserves) severely hinder their availability in practical industrial applications.[13,14] Therefore, there is an urgent need to develop a non-precious metal-based HER electrocatalyst with high efficiency, acid resistance, and long-term stability. In particular, metal cluster/single-atom catalysts have received widespread attention due to the ability to use metal clusters to tune the electronic structure of single atoms.[15–17] Generally, the increase of the metal content could effectively improve the HER electrocatalytic performance of the catalyst, while the excess metal is prone to agglomeration during the pyrolysis process, thereby seriously reducing the HER activity of the catalyst.[18,19] Therefore, improving the intrinsic activity of a single active site is an effective way to enhance the electrocatalytic activity for the HER. It has been reported that carbides, such as molybdenum carbide[20] and manganese carbide,[21] are superior HER electrocatalysts with excellent electrical conductivity, resistance to acid, and alkali environments, and exhibit excellent long-term HER stability. Specifically, carbide clusters could induce changes in the local electronic structure, and reduce the adsorption energy of H* and the energy barrier of H* activation by regulating the

[a]College of Resources and Environment, University of Chinese Academy of Sciences, 19A Yuquan Road, Beijing 100049, P. R. China. E-mail: yuzs@ucas.ac.cn; Fax: +86-10-88256057; Tel: +86-10-88256057

[b]Binzhou Institute of Technology, Weiqiao-UCAS Science and Technology Park, Binzhou City 256606, Shandong Province, P. R. China

[c]RCEES-IMCAS-UCAS Joint-Lab of Microbial Technology for Environmental Science, Beijing 100085, China

† Electronic supplementary information (ESI) available. See DOI: https://doi.org/10.1039/d3sc06053e

electron density of d orbitals and TDOS.[22,23] Besides, the introduction of metal single-atom sites could not only regulate the surrounding electronic structure but also serve as the adsorption sites of H*, which facilitate the adsorption/desorption of H* and reduce the energy barrier of the HER process.[24,25] Based on the above analysis, it was speculated that the coupling of metal clusters and single atoms might exhibit unexpected HER electrocatalytic properties. Most of the current studies mainly focus on the optimization of the active sites of single atoms and metal clusters, and there are a large number of reports on the synergistic effect between single atoms and metal clusters.[26–29] Non-noble metals including Mo and Mn have been proven to exhibit good performance in electrocatalytic hydrogen evolution. The pyrolysis of Mo and C in a reducing atmosphere could generate Mo_xC. Mo_xC has a d-band electronic structure similar to Pt, and its flexible controllability and high conductivity ensure its high activity and stability in a wide pH range, thus showing promise as an HER catalyst.[11,30] Mn single atoms are an efficient candidate in the research of manganese-based catalyst materials and could be used in many challenging catalytic reactions. The three-dimensional unoccupied orbitals in Mn single atoms could accommodate foreign electrons, thereby effectively reducing the bonding strength with H* intermediates during the HER process. In addition, the introduction of Mn single atoms in carbon-based catalysts could promote the formation of Mn–N–C and enhance HER catalytic activity and stability.[15] Previous studies reported that the coupling of Mo_xC with metals or non-metals is an effective method to improve the kinetics and activity of the HER.[31] There are relatively few studies on electrocatalysts with the synergistic effects of Mo and Mn doped together in biochar. How the coordination conditions or structures between Mo_xC and Mn single atoms affect the HER performance is still a question that needs to be explored. Therefore, it is necessary to further evaluate the HER performance of the catalyst formed by the two and explore its HER mechanism.

Herein, a novel biochar-based HER electrocatalyst ($BC_{MoMn800\text{-}2}$) with Mo_2C/Mn_7C_3 clusters and atomically dispersed MnN_4 was prepared from *in situ* enriched Mo/Mn biomass as a precursor. HAADF-STEM and X-ray absorption near-edge spectroscopy results demonstrate the formation of atomically dispersed MnN_4 single atoms and Mo_2C/Mn_7C_3 clusters. Density functional theory (DFT) calculations further elucidated the strong electronic interaction between Mo_2C/Mn_7C_3 clusters and single-atom Mn sites, as well as the electrocatalytic mechanism of the HER. According to the above structural features, $BC_{MoMn800\text{-}2}$ exhibited excellent electrocatalytic activity for the HER. In 0.5 M sulfuric acid, the overpotential was 27.4 mV at a current density of 10 mA cm^{-2} and the Tafel slope was 31 mV dec^{-1}, thus the electrocatalytic performance was close to that of Pt/C. Moreover, excellent long-term stability and durability were exhibited. Overall, experiments and theoretical calculations confirmed that $BC_{MoMn800\text{-}2}$ with metal clusters and single atoms is a low-cost and promising electrocatalyst for the HER.

Results and discussion

Characterization of electrocatalysts

The evolution of the catalyst structure at different pyrolysis temperatures is shown in Fig. 1a. In this study, biomass precursors containing Mo and Mn were prepared by plant absorption and further pyrolyzed at 700, 800, and 900 °C to obtain BC_{MoMn} with a graphene-like structure and abundant defects. Notably, the preparation method of BC_{MoMn} precursors using plant-absorbed metal ions displayed the following advantages. (1) Unlike the conventional impregnation pyrolysis method, this preparation method was beneficial for the uniform distribution of metal elements in biochar. (2) Evenly distributed metal elements were beneficial to the regulation of the local microenvironment of the catalyst. (3) N absorbed during plant growth enhanced the formation of metal single atoms during pyrolysis.

The crystalline phases of the synthesized catalysts were detected by X-ray diffraction (XRD). As illustrated in Fig. 1b and S1,† an obvious characteristic diffraction peak was observed at 26.4° in all samples, which matched with graphitic carbon (C, PDF#41-1487).[24] With the increase of pyrolysis temperature, the intensity of the diffraction peak gradually increased, indicating that high temperature could transform amorphous carbon into graphitic carbon under the action of Mn/Mo. More importantly, XRD results demonstrated the formation of Mo_2C and Mn_7C_3 in the synthesized samples. Characteristic diffraction peaks of Mo_2C (PDF#35-0787) at 2θ = 38.0, 39.4, 52.1, 61.5, 69.6, 74.6, and 75.5° are ascribed to the (002), (101), (102), (110), (103), (112), and (201) facets, respectively.[32] Additionally, characteristic diffraction peaks of Mn_7C_3 (PDF#36-1269) at 2θ = 44.6, 45.3, 49.8, 50.3, and 52.8° are ascribed to the (211), (300), (301), (202), and (220) facets, respectively.[33] Notably, after increasing the temperature to 900 °C, the diffraction peak of Mn_7C_3 almost disappeared, which may be due to the fact that Mn_7C_3 clusters participated in the growth of the carbon layer during the high-temperature graphitization of biochar.[34] Combining XRD patterns analyzed from samples pyrolyzed at 600 °C (Fig. S1b†) and the literature,[35,36] it could be speculated that the Mo^0/Mn^0 formed by reduction at 600 °C acted as a catalyst to start promoting the formation of graphene-like structure. By increasing the temperature to 700–800 °C, the Mo^0/Mn^0 gradually transformed into Mo_2C/Mn_7C_3 and were gradually wrapped by graphene-like structure. By further raising the temperature to 900 °C, Mn_7C_3 clusters were gradually consumed and combined in the stable form of graphene-like structure and Mn_7C_3.

The microstructure of the synthesized samples was characterized by field-emission scanning electron microscopy (FESEM), transmission electron microscopy (TEM), high-resolution transmission electron microscopy (HRTEM) and high-angle annular dark-field scanning transmission electron microscopy (HAADF-STEM). FESEM results showed that the $BC_{MoMn800\text{-}2}$ sample possessed a smooth surface structure (Fig. 1c). Compared with the control biochar, the introduction of Mn/Mo did not induce obvious changes in the morphology of

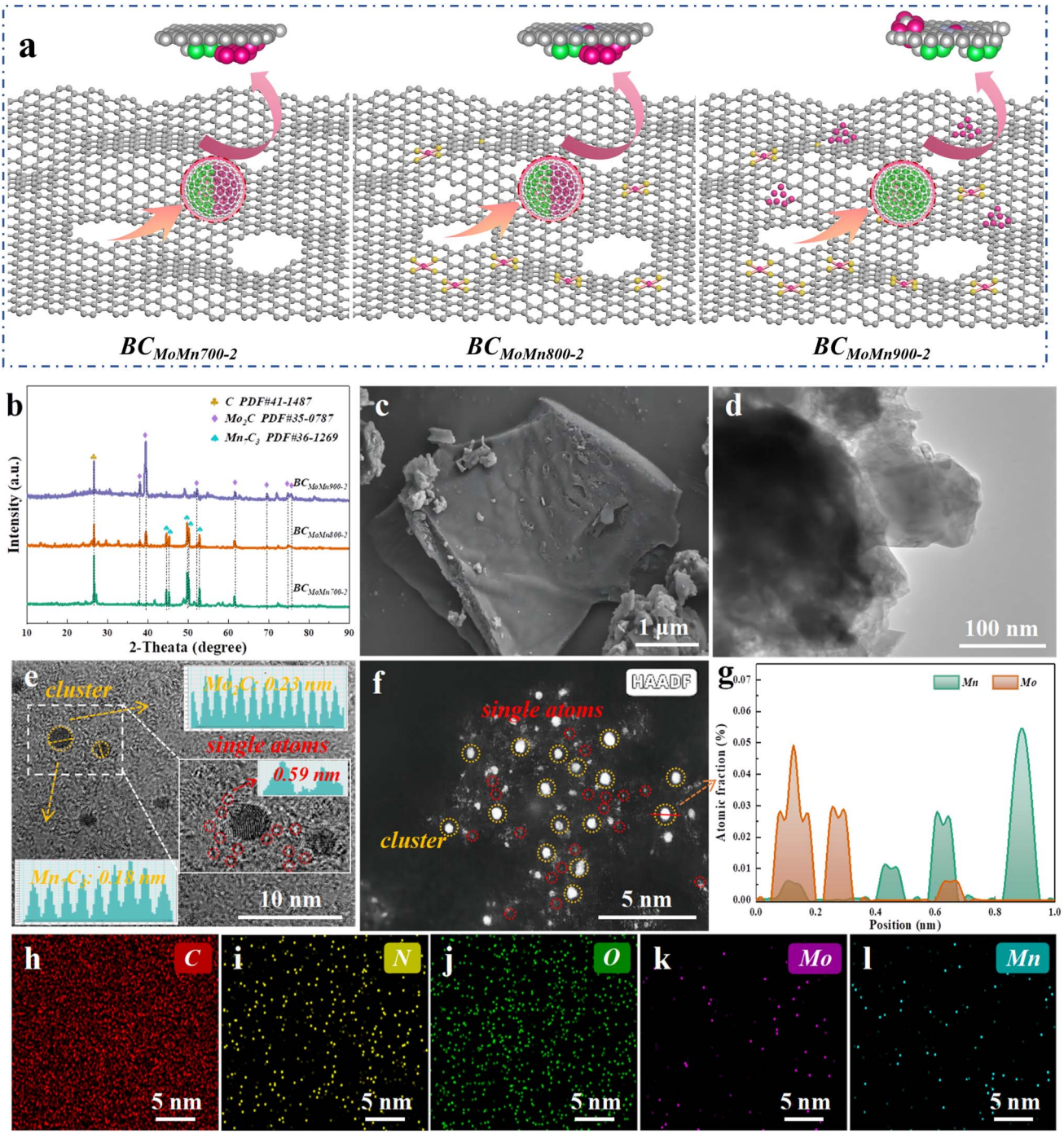

Fig. 1 Catalyst synthesis and structural characterization. (a) Schematic illustration of catalyst structure evolution at different preparation temperatures. (b) XRD spectra of $BC_{MoMn700\text{-}2}$, $BC_{MoMn800\text{-}2}$, and $BC_{MoMn900\text{-}2}$. (c) FESEM, (d) TEM, (e) HRTEM, (f) dark-field HAADF-STEM, (g) corresponding EDS line-scan elemental of $BC_{MoMn800\text{-}2}$, and (h–l) EDS mappings of $BC_{MoMn800\text{-}2}$.

biochar. Additionally, TEM images further confirmed the smooth surface structure of $BC_{MoMn800\text{-}2}$ (Fig. 1d). These results indicated that the preparation method achieved a uniform distribution of Mn/Mo in biochar, thereby suppressing the agglomeration of metal nanoparticles during pyrolysis. The HRTEM image clearly exhibited the metal cluster size (only 0.5–1.5 nm) and lattice fringe properties on the biochar substrate (yellow circles and split lines highlighted, Fig. 1e). Notably, two kinds of lattice fringes could be observed with distinct interfaces (dashed yellow lines highlighted). According to the Fast Fourier Transform (FFT) of the cluster lattice fringes (Fig. 1e inset), lattice spacings of 0.23 and 0.18 nm were calculated, corresponding to the (003) crystal plane of Mo_2C and (004) crystal plane of Mn_7C_3, respectively. As reported, the preparation method of plant enrichment could achieve a uniform distribution of metal species in biochar rather than loading

them on the surface.[37] Of note, obvious carbon stripes were observed at the edge of the lattice (Fig. 1e inset), suggesting that the Mo_2C/Mn_7C_3 clusters were wrapped by the carbon layer. The distance between close bright spots was 0.59 nm (Fig. 1e inset), which was significantly larger than the atomic diameter of Mo/Mn atoms (0.278/0.254 nm), suggesting that the Mo or Mn element was distributed as a single atom in $BC_{MoMn800\text{-}2}$.[38] The HAADF-STEM images clearly revealed metal single atoms (highlighted in red circles) and clusters (highlighted in yellow circles) on the biochar matrix (Fig. 1f), indicating the coexistence of single-atom dispersed M–N–C sites and metal clusters.[39] The positional relationship of Mo/Mn in metal clusters was further proved by EDS line-scan elemental of $BC_{MoMn800\text{-}2}$ (Fig. 1g), which was consistent with FFT analysis. Additionally, the energy-dispersive X-ray spectroscopy (EDS) images of $BC_{MoMn800\text{-}2}$ confirmed the uniform distribution of N, Mo, and Mn elements on the biochar. More details on electron microscopy characterization of other catalysts are provided in Fig. S2.†

The carbon structural defects of the synthesized catalysts were characterized by Raman spectroscopy. The peaks at 1350 (D band) and 1580 (G band) cm^{-1} were ascribed to defective/disordered carbon and graphitic structures, respectively, while the ratio of D and G bands (I_D/I_G) could reflect the defect degree of carbon-based materials.[40] As reported, different metal crystalline phases could lead to differences in the structural defects of carbon layers.[41] By calculation, the I_D/I_G values of $BC_{MoMn700\text{-}2}$, $BC_{MoMn800\text{-}2}$, and $BC_{MoMn900\text{-}2}$ were 1.00, 1.12, and 1.07 (Fig. 2a), respectively, indicating that more carbon defect structures were formed in $BC_{MoMn800\text{-}2}$, which were conducive to the adjustment of the surface electronic structure, thereby enhancing the interfacial electron exchange.[42] Additionally, the loading amount of Mo/Mn also affected the structure of the carbon (Fig. S3 and Table S1†). The I_D/I_G values of $BC_{MoMn800\text{-}1}$ and $BC_{MoMn800\text{-}3}$ were 1.05 and 1.18, suggesting that carbon structural defects gradually increased as the content of Mo and Mn increased.

The surface elemental composition and chemical speciation of the synthesized catalysts were detected by X-ray photoelectron spectroscopy (XPS). XPS further confirmed the existence of C, O, N, Mo, and Mn elements on the catalyst's surface (Fig. S4a†). Specifically, all synthesized catalysts exhibited similar C 1s and O 1s XPS spectra (Fig. S4b and c†). As illustrated in Fig. 2b, the high-resolution N 1s spectra of $BC_{MoMn700\text{-}2}$ were fitted with four peaks at 403.1, 400.8, 400.0, and 398.4 eV, corresponding to oxidized-N, graphitic-N, pyrrolic-N, and pyridinic-N.[43,44] Notably, the high-resolution N 1s spectra of $BC_{MoMn800\text{-}2}$ and $BC_{MoMn900\text{-}2}$ were fitted with a Mn–N peak at 399.3 eV and 399.8 eV instead of the pyrrolic-N peak,[45] and the negative electron shift of 0.5 eV indicated that $BC_{MoMn800\text{-}2}$ possessed a higher N electron density than $BC_{MoMn900\text{-}2}$. Additionally, $BC_{MoMn800\text{-}2}$ exhibited a higher relative content of graphite-N (42.6%) and Mn–N (21.4%) than the others (in Table S2†), which was beneficial for the accelerated electron transfer during the HER, thereby increasing the current density.[46,47] The high-resolution Mo 3d spectra of $BC_{MoMn700\text{-}2}$ could be fitted with three groups of peaks at 228.0/231.0, 228.5/232.1, and 232.2/235.3 eV (Fig. 2c), corresponding to Mo_2C, MoO_2, and MoO_3,[31,48] where MoO_2 and MoO_3 may be caused by surface oxidation.[49,50] In particular, the Mo_2C peaks in $BC_{MoMn800\text{-}2}$ and $BC_{MoMn900\text{-}2}$ were positively shifted by 0.4 and 0.2 eV, indicating that Mo_2C on $BC_{MoMn800\text{-}2}$ exhibited a significantly electron-deficient feature than the other two. The high-resolution Mn 2p spectra of $BC_{MoMn700\text{-}2}$ could be fitted with two groups of peaks at 641.2/653.1 and 642.5/654.0 eV (Fig. 2d), which were ascribed to Mn^{2+} and Mn^{3+}, respectively.[45] Similarly, the Mn 2p spectra of $BC_{MoMn800\text{-}2}$ and $BC_{MoMn900\text{-}2}$ exhibited a positive shift, especially $BC_{MoMn800\text{-}2}$ (0.3 eV), indicating the electron loss tendency on Mn sites.[51,52] According to the above results, it could be speculated that the Mn single atoms on the graphene-like structure could promote the electron transfer from the Mo_2C/Mn_7C_3 clusters to the graphene-like structure, thereby resulting in the strengthening of electronic metal–support interaction between the Mo_2C/Mn_7C_3 clusters and the carbon layer. This speculation was further confirmed by DFT calculations (Fig. S5–S7†).

The electronic structures and coordination environments of Mo and Mn species in $BC_{MoMn800\text{-}2}$ were detected by X-ray absorption fine structure spectroscopy (XAFS). As illustrated in Fig. 2e, the Mo k-edge X-ray absorption near-edge structure (XANES) spectrum showed that the absorption edge position of Mo in $BC_{MoMn800\text{-}2}$ was between Mo foil and MoO_2, indicating that the average valence state of Mo was between 0 and +4. Moreover, Fourier-transformed X-ray absorption fine structure (FT EXAFS) of Mo k-edge revealed obvious Mo–C and Mo–Mo coordination at 1.3 and 2.4 Å (Fig. 2g), further confirming the generation of Mo_2C in $BC_{MoMn800\text{-}2}$.[53] Additionally, the weak Mo–O (1.7 Å) coordination may be due to the surface oxidation of the sample in air. As illustrated in Fig. 2f, the Mn k-edge XANES spectrum of $BC_{MoMn800\text{-}2}$ was in the vicinity of Mn_2O_3, indicating that the valence state of Mn was around +3. In the analysis of Mn k-edge FT EXAFS (Fig. 2h), the peaks at 1.4 and 2.3 Å could be ascribed to Mn–C and Mn–Mn coordination, which were the key to prove the existence of Mn_7C_3.[33,54] More importantly, the Mn–N coordination at 1.7 Å was detected in FT EXAFS of $BC_{MoMn800\text{-}2}$.[55] As reported,[16] due to the complexity of metal–nitrogen–carbon materials, the average coordination number between the metal and nitrogen could not directly prove the specific structure of Metal–N_x. The calculated average coordination number of Mn–N was about 2.0, which may be due to the reduction of the coordination number of N by the Mn atoms adjacent to the cluster heterojunction. Notably, Mo–Mn coordination was also detected at 2.1 Å in the FT EXAFS of both Mo and Mn k-edges, which could be due to the interfacial coupling of clusters formed by Mo_2C and Mn_7C_3. Combined with HAADF-STEM and XRD analysis, it was further confirmed that Mo_2C and Mn_7C_3 in $BC_{MoMn800\text{-}2}$ existed in the form of clusters instead of nanoparticles. The wavelet transform (WT) of the k^3-weighted EXAFS spectrum could further reconfirm the above coordination structure (Fig. 2i). According to the above results, it was inferred that the possible structure of $BC_{MoMn800\text{-}2}$ was MnN_4 fixed on the graphene layer plane and Mo_2C/Mn_7C_3 clusters below the graphene layer. This structure contained 4 Mn–N bonds and 2 Mn atoms (Fig. 2i inset), so the average coordination number of Mn–N was about 2.0, which was consistent with the detection and calculation results. Mn–N

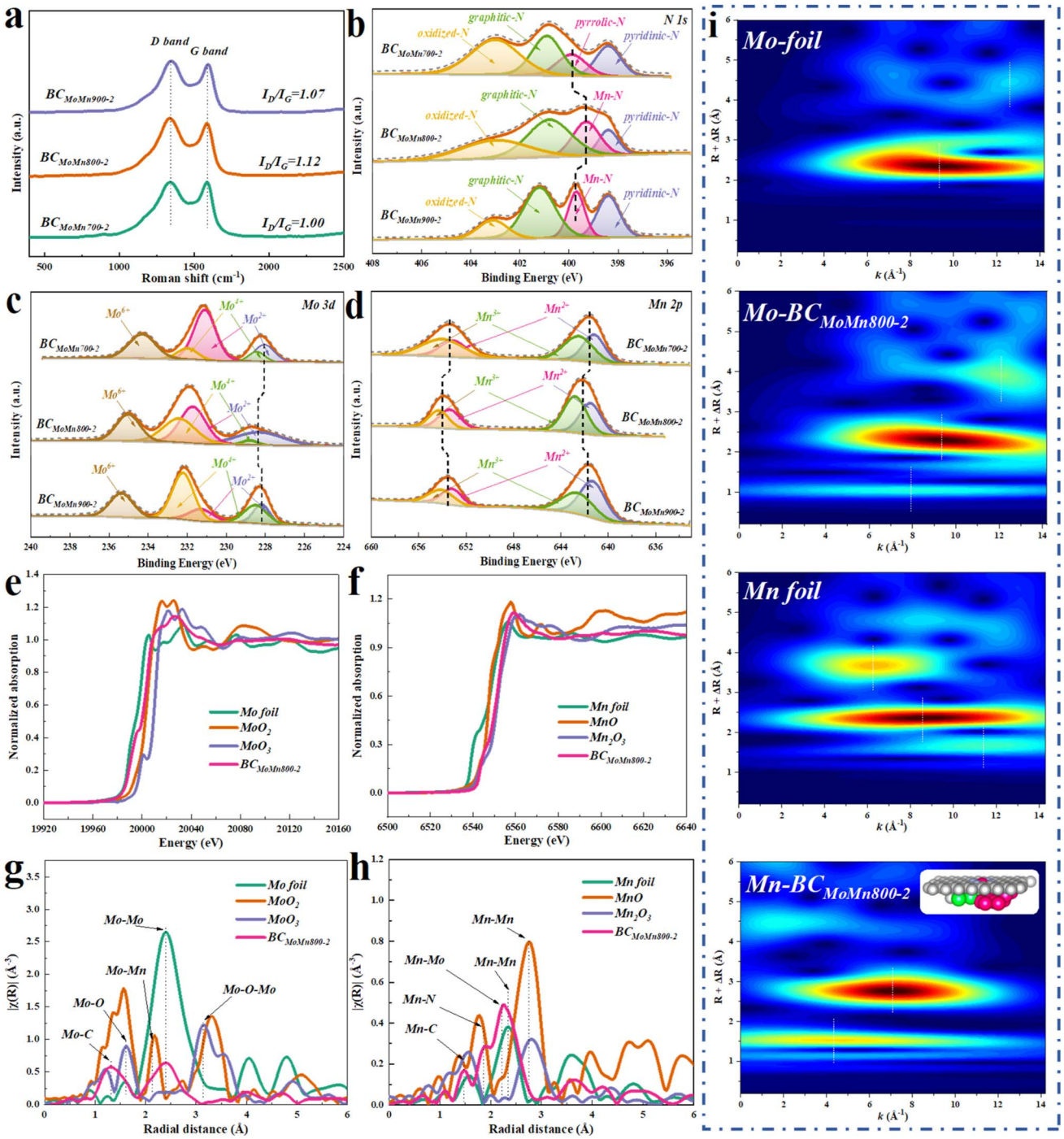

Fig. 2 Chemical composition characterization. The (a) Raman, (b) high-resolution Mo 2p, (c) Mn 2p, and (d) N 1s spectra of $BC_{MoMn700-2}$, $BC_{MoMn800-2}$, and $BC_{MoMn900-2}$. (e, g) Mo and (f, h) Mn K-edge XANES and Fourier transforms of the EXAFS spectra of $BC_{MoMn800-2}$. (i) Wavelet transforms for the k^3-weighted EXAFS signals of Mo foil, Mn foil, and $BC_{MoMn800-2}$.

also existed in $BC_{MoMn900-2}$, but not in $BC_{MoMn700-2}$ (Fig. S8†). It was speculated that Mn single atoms were generated when the pyrolysis temperature was greater than 700 °C.[56] Moreover, Mn single atoms could facilitate the electron transfer from the Mo_2C/Mn_7C_3 cluster to the graphene-like structure by DFT calculation, thereby enhancing the electronic metal–support interaction (Fig. S6†).

HER catalytic performances

To evaluate the HER electrocatalytic performance of the synthesized catalysts, electrochemical tests were performed in 0.5 M H_2SO_4 electrolyte. As illustrated in Fig. 3a, the linear sweep voltammetry (LSV) image revealed that $BC_{MoMn800-2}$ exhibited a higher current density than others, indicating its superior HER catalytic performance. Notably, at a current density of 10 mA

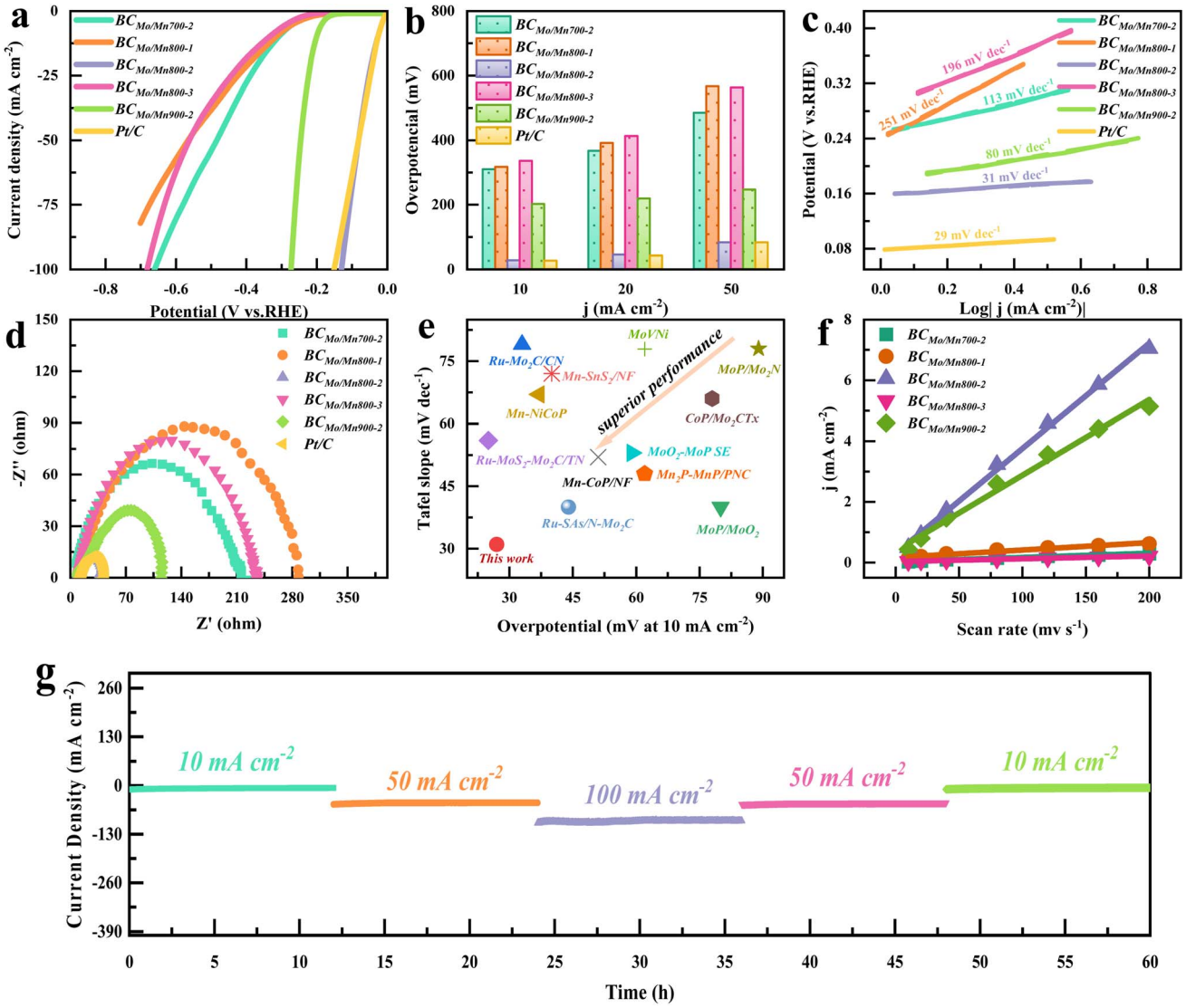

Fig. 3 Electrochemical HER performance in 0.5 M H_2SO_4 solution. (a) HER polarization curves, (b) comparison of overpotential changes, (c) the corresponding Tafel plots, and (d) electrochemical impedance spectroscopy of $BC_{MoMn700\text{-}2}$, $BC_{MoMn800\text{-}1}$, $BC_{MoMn800\text{-}2}$, $BC_{MoMn800\text{-}3}$, $BC_{MoMn900\text{-}2}$, and Pt/C. (e) Comparison of the Tafel slope and overpotential at 10 mA cm^{-2} for $BC_{MoMn800\text{-}2}$ with other recently reported HER catalysts. (f) The differences in current density ($\Delta j_{1/2}$) at 0.118 V (*vs.* RHE) as a function of scan rate for HER catalysts. (g) The electrolysis stability test of $BC_{MoMn800\text{-}2}$ at different current densities in 0.5 M H_2SO_4.

cm^{-2} (Fig. 3b), the overpotential of $BC_{MoMn800\text{-}2}$ was only 27.4 mV, which was close to that of Pt/C (26.4 mV), but much lower than that of $BC_{MoMn700\text{-}2}$ (309.4 mV), $BC_{MoMn800\text{-}1}$ (316.4 mV), $BC_{MoMn800\text{-}3}$ (335.4 mV), and $BC_{MoMn900\text{-}2}$ (201.4 mV). Additionally, even at current densities of 20, 50, and 100 mA cm^{-2}, $BC_{MoMn800\text{-}2}$ still exhibited smaller overpotentials than other catalysts. Subsequently, the HER kinetics of the catalysts were evaluated by calculating the Tafel slope (Fig. 3c). The Tafel slope of $BC_{MoMn800\text{-}2}$ was the smallest, only 31 mV dec^{-1}, which was much smaller than that of $BC_{MoMn700\text{-}2}$ (113 mV dec^{-1}), $BC_{MoMn800\text{-}1}$ (251 mV dec^{-1}), $BC_{MoMn800\text{-}3}$ (196 mV dec^{-1}), and $BC_{MoMn900\text{-}2}$ (80 mV dec^{-1}), and close to that of Pt/C (29 mV dec^{-1}). These results indicated that the HER process of the catalysts followed the Volmer–Heyrovsky mechanism, and the Tafel step was rate-limiting.[57] Electrochemical impedance spectroscopy (EIS) further revealed the interfacial electron transfer kinetics of the catalysts in the HER process (Fig. 3d), and the resistance of $BC_{MoMn800\text{-}2}$ was the smallest (only 27.38 Ω), indicating the fastest charge transfer at the interface with the electrolyte. Compared with some of the recently reported advanced Mo/Mn catalysts, $BC_{MoMn800\text{-}2}$ exhibited excellent overpotential and Tafel slope in the HER process compared with the recently reported advanced Mo/Mn-containing catalysts (Fig. 3e).

To evaluate the abundance of active sites, the effective electrochemical surface area (ECSA) of the catalyst was detected by the electrochemical double-layer capacitance method (Fig. 3f and S9†). Among the synthesized catalysts, $BC_{MoMn800\text{-}2}$ possessed the largest double-layer capacitance of 34.6 mF cm^{-2}, indicating its larger ECSA and more abundant active sites than

others. Overall, from the overpotential, Tafel slope, resistance, and ECSA, it could be obviously shown that $BC_{MoMn800\text{-}2}$ exhibited superior catalytic activity in the HER process. The HER performance of electrodes is not only related to ECSA, but also affected by electrode composition, active surface area, and hydrophilicity.[58] Among them, the hydrophilicity of the electrode surface is a key factor affecting the movement behavior of H_2 bubbles, thus determining the kinetic performance of the HER reaction. In principle, the formation of small uniform H_2 bubbles facilitates its desorption from the electrode without causing polarization of the electrode. The contact angles of $BC_{MoMn800\text{-}2}$ were 32.6, 27.1, 24.0, 19.8, and 14.3° at 0, 100, 200, 500, and 1000 ms, respectively, which exhibited excellent hydrophilicity (Fig. S10†). The optimal hydrophilicity of the $BC_{MoMn800\text{-}2}$ electrode might be due to its abundant mesopores, channels, and defect structures, which accelerated the separation of the generated H_2 bubbles and enabled the acidic electrolyte to reach the active catalytic sites.[59] From Fig. S11,† the electrode surface of $BC_{MoMn700\text{-}2}$ and $BC_{MoMn900\text{-}2}$ adsorbed a large number of large bubbles generated, resulting in the coverage of active sites on the catalyst surface, thereby reducing the mass transfer rate at the electrode/electrolyte interface. In contrast, the electrode surface of $BC_{MoMn800\text{-}2}$ generated uniform small bubbles and desorbed rapidly, exhibiting superior H_2 production efficiency. Therefore, electrodes with smaller contact angles were beneficial for the generation of small/uniform bubbles and their rapid desorption from the electrode surface, thereby maintaining the mass transfer rate at the electrode/electrolyte interface, the effectiveness and stability of electrode activity.[60]

Cyclic voltammetry (CV) tests were performed to evaluate the electrochemical stability of $BC_{MoMn800\text{-}2}$ during the acidic HER process. After 1000 cycles, HER polarization curves changed slightly, indicating its superior electrochemical stability (Fig. S12†). Additionally, further characterization analysis of the tested materials (Fig. S13 and S14†), including SEM, TEM, XRD, *etc.*, showed that the surface of $BC_{MoMn800\text{-}2}$ maintained good microstructure and crystal phase characteristics. These results indicated that $BC_{MoMn800\text{-}2}$ exhibited superior electrochemical stability during the HER process. Long-term electrolytic stability tests at different current densities were performed to further evaluate the application prospect in the actual process (Fig. 3g). During the continuous experiment of 60 h, even if different current densities were applied, the current density of the reaction system remained stable. Notably, at a current density of 10 mA cm^{-2}, the current density of the $BC_{MoMn800\text{-}2}$ system decreased by less than 10%, indicating its excellent electrochemical stability for acidic HER, showing broad application prospects.

To evaluate the HER electrocatalytic active sites of the synthesized catalysts, the turnover frequency (TOF) was calculated. As illustrated in Fig. S15,† at an overpotential of 250 mV, the $BC_{MoMn800\text{-}2}$ electrode exhibited a superior TOF value of 74.2 s^{-1} compared to other electrodes, indicating that the $BC_{MoMn800\text{-}2}$ electrode possessed an excellent intrinsic HER electrocatalytic activity. Combined with characterization analysis, this may be due to the synergy between Mo_2C–Mn_7C_3 clusters and MnN_4. In detail, Mo_2C–Mn_7C_3 clusters on $BC_{MoMn800\text{-}2}$ provided electrons for H* activation, while MnN_4 on graphene was beneficial for electron aggregation and H* adsorption/desorption. It is known that the HER activity of catalysts is not only dependent on the type of active sites but also closely related to the number and size of active sites. Compared with $BC_{MoMn800\text{-}2}$, $BC_{MoMn800\text{-}1}$ exhibited a lower electrocatalytic activity for the HER, which may be attributed to the lower number of active sites due to lower metal loading.[61] In contrast, $BC_{MoMn800\text{-}3}$ possessed a higher metal content (Table S1†), but its HER electrocatalytic activity was significantly lower than that of $BC_{MoMn800\text{-}2}$, which might be due to the agglomeration of Mo_2C–Mn_7C_3 clusters caused by the excessive metal loading, reducing the HER electrocatalytic activity of the catalyst. Moreover, from the SEM and HRTEM images (Fig. S2†), the particle size of $BC_{MoMn800\text{-}3}$ was significantly increased compared to that of $BC_{MoMn800\text{-}2}$, demonstrating that the increase of particle size suppressed the electrocatalytic activity of the HER, thus further proving the speculation.

Mechanism and theoretical calculation

To elucidate the mechanism of the superior HER activity of the synthesized catalysts from the atomic scale, DFT calculations were performed. Based on HAADF-STEM and XAFS characterization analysis, the atomic models of Mo_2C–Mn_7C_3/graphene, Mo_2C–Mn_7C_3/MnN_4-graphene, and Mo_2C/Mn_7C_3–MnN_4-graphene were constructed and optimized (Fig. 4a and S5†), corresponding to $BC_{MoMn700\text{-}2}$, $BC_{MoMn800\text{-}1}$, and $BC_{MoMn900\text{-}2}$, respectively. As reported,[62] a positive value of the Gibbs free energy of H* adsorption indicated that the HER catalyst exhibited poor adsorption of H*, while a negative value might result in difficulty in the desorption of the generated H_2 molecules. In acidic systems, among Mo_2C–Mn_7C_3/graphene, Mo_2C–Mn_7C_3/MnN_4-graphene, and Mo_2C/Mn_7C_3–MnN_4-graphene, Mo_2C–Mn_7C_3/MnN_4-graphene exhibited the best Gibbs free energy of H* adsorption ($\Delta G_{H^*} = -0.03$ eV, Fig. 4b), which was almost close to the ideal value of 0, indicating its excellent H* adsorption/desorption kinetics.[63] Notably, from the charge density difference diagram, the Mo_2C–Mn_7C_3 heterostructure formed in Mo_2C–Mn_7C_3/MnN_4-graphene exhibited a large local lattice distortion, resulting in changes in the local electronic structure, thereby increasing the activity of electrons. The Bader charge analysis further demonstrated the superior electron donating ability of the Mo_2C–Mn_7C_3 heterojunction (−0.293 e) compared to Mo_2C (−0.197 e, Fig. S6†), and electrons were transferred from Mo_2C–Mn_7C_3 to graphene, which was consistent with XPS analysis. Moreover, the density of states (DOS) at the Fermi level of the metal d orbitals in the Mo_2C–Mn_7C_3 heterostructure was significantly weakened (Fig. S7†), thereby resulting in a weakened adsorption capacity. Besides, the MnN_4 on graphene enhanced the charge transfer from Mo_2C–Mn_7C_3 to the graphene layer.

Moreover, the electron transfer of different models during the H* adsorption process was investigated. H atoms adsorbed on Mo_2C–Mn_7C_3/MnN_4-graphene exhibited a smaller charge transfer of −0.148 e than Mo_2C–Mn_7C_3/graphene and Mo_2C/

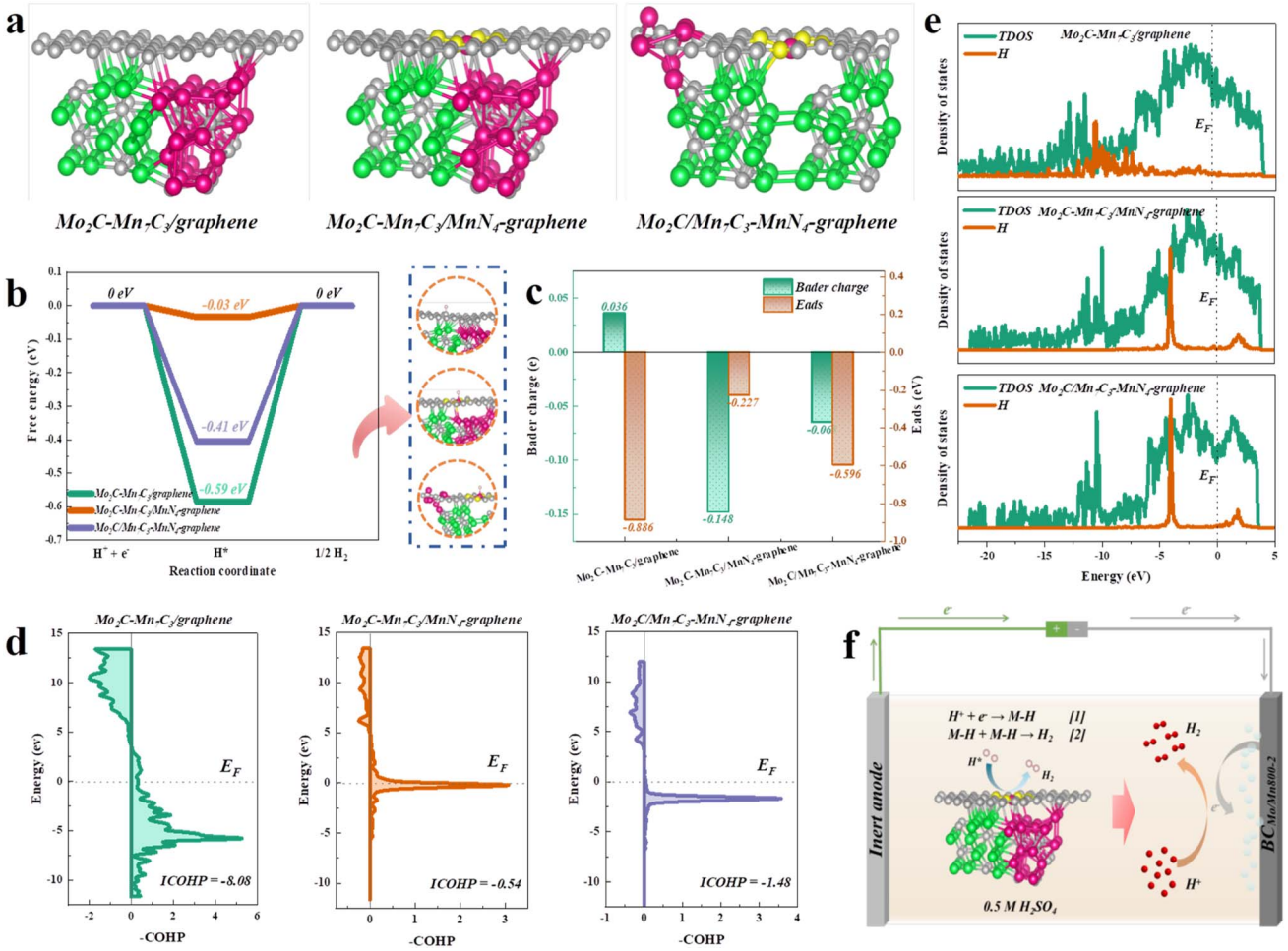

Fig. 4 DFT calculations. (a) Optimized atomic structures of Mo_2C–Mn_7C_3/graphene, Mo_2C–Mn_7C_3/MnN_4-graphene, and Mo_2C/Mn_7C_3–MnN_4-graphene. (b) The Gibbs free energy diagrams of the HER in an acid electrolyte at the equilibrium potential (inset: DFT calculations of H^+ adsorption on different substrates). Calculation of (c) Bader charge, adsorption energies, (d) COHP, and (e) PDOS for H* adsorption on Mo_2C–Mn_7C_3/graphene, Mo_2C–Mn_7C_3/MnN_4-graphene, and Mo_2C/Mn_7C_3–MnN_4-graphene. (f) Schematic diagram of the HER mechanism.

Mn_7C_3–MnN_4-graphene, corresponding to the smaller adsorption energy (E_{ads}) of −0.227 eV (Fig. 4c). The charge transfer of H atoms exhibited a significant linear relationship with E_{ads} (R^2 = 0.98, Fig. S16†), indicating that the low charge transfer on hydrogen atoms resulted in the weaker adsorption of H*, thereby accelerating the desorption of H*.

To evaluate the contribution of the bonding and antibonding states of H uptake at the Mo_2C–Mn_7C_3/MnN_4-graphene interface, the projected crystal orbital Hamilton population (pCOHP) analysis was performed.[64] The integral COHP (ICOHP) of Mo_2C–Mn_7C_3/MnN_4-graphene was maximum (−0.54 *vs.* −8.08 of Mo_2C–Mn_7C_3/graphene, −1.48 of Mo_2C/Mn_7C_3–MnN_4-graphene) in all models (Fig. 4d), corresponding to a moderate bonding strength, which was more conducive to the dissociation of H*. Moreover, the overlapping peaks of the H partial density of states on Mo_2C–Mn_7C_3/MnN_4-graphene were more pronounced than Mo_2C–Mn_7C_3/graphene and Mo_2C/Mn_7C_3–MnN_4-graphene in the PDOS calculations (Fig. 4e), indicating that it was closer to the Fermi level. So, it was more favorable for the activation of H atoms. Overall, these theoretical results indicated the synergistic effect between Mo_2C–Mn_7C_3 clusters and MnN_4 to accelerate the adsorption/dissociation of H*, resulting in its excellent HER performance in acidic solution. Correspondingly, a schematic diagram of the HER mechanism is proposed, as shown in Fig. 4f.

Conclusion

In summary, Mo/Mn biochars (BC_{MoMn}) were prepared from *in situ* enriched Mo/Mn biomass as precursors at different pyrolysis temperatures, especially at 800 °C. The synthesized $BC_{MoMn800\text{-}2}$ exhibited excellent HER electrocatalytic activity. In an acidic electrolyte, the overpotential of $BC_{MoMn800\text{-}2}$ was 27.4 mV at a current density of 10 mA cm^{-2}, and the Tafel slope was 31 mV dec^{-1}, which was close to that of Pt/C. This was ascribed to the unique properties arising from the interaction between MnN_4 and Mo_2C/Mn_7C_3 clusters in $BC_{MoMn800\text{-}2}$. DFT calculations revealed that the heterojunction of Mo_2C/Mn_7C_3 clusters in $BC_{MoMn800\text{-}2}$ induced changes in the local electronic structure and charge redistribution of the clusters. It was an indirect electron transfer, resulting in a decrease in charge at the MnN_4 site and an increase

in electron density around C–N. Moreover, the presence of Mo_2C/Mn_7C_3 clusters reduced the energy required for H* activation and indirectly facilitated the desorption of H*. Crucially, the optimized electronic structure of MnN_4 sites facilitated the adsorption/desorption of H*, thereby promoting the kinetic process of the HER. These results indicated that $BC_{MoMn800\text{-}2}$ exhibited superior electrocatalytic performance for the HER to that of $BC_{MoMn700\text{-}2}$ and $BC_{MoMn900\text{-}2}$, which might be mainly derived from the synergistic effect of MnN_4 and Mo_2C/Mn_7C_3 clusters rather than the pure increase of metal content. In this study, we successfully synthesized an efficient and stable HER electrocatalyst, clarified the synergy and catalytic mechanism between clusters and single atoms, and provided a new idea for solid waste recycling and the synthesis of electrocatalysts.

Experimental section

Materials

Anhydrous ethanol (AR, 99.7%) and Nafion117 solution (5 wt%) were purchased from Aladdin Holdings Group Co., Ltd. Hoagland nutrient solution was purchased from Fuzhou Feijing Biological Technology Co., Ltd. Sodium molybdenum oxide (Na_2MoO_4, 99%), manganese chloride ($MnCl_2$, 99%) and platinum on carbon (Pt/C, 20%wt) were obtained from Meryer (Shanghai) Chemical Technology Co., Ltd. Sulfuric acid (H_2SO_4, AR) was purchased from Beijing Chemical Co., Ltd. All chemicals were of analytical grade and used as received without further purification.

Synthesis of biochar electrocatalysts *in situ* doped with Mo_2C and single-atomic Mn

The source of electrocatalysts: Reed seedlings were bought with the same biological quality, the roots of reed seedlings were rinsed with running water, and then fixed with white stones into buckets. Subsequently, they were cultured with Hoagland nutrient solution, Na_2MoO_4 and $MnCl_2$ (300, 500, and 800 mg L^{-1}), and changed every week to ensure the concentration of Mo and Mn ions, which would last for three months. The reed roots were washed with deionized water several times after the completion of growth, and the biomass containing Mo and Mn ions was obtained by drying for 24 h. The reeds were crushed with a grinder for 5 min before use.

Synthesis of Mo_2C, Mn_3C_7, and single-atomic Mn nanostructures: The required electrocatalysts were obtained by the pyrolysis of biomass in a vacuum tube furnace at 700, 800, and 900 °C for 2 h, the pyrolysis rate was 3 °C min^{-1}. The obtained biochar was stirred in 1 M H_2SO_4 for 24 h and then pumped and filtered to obtain a black solid, which was washed with deionized water several times until it approached the pH of deionized water. After that, the extracted biochar was dried for 48 h at a temperature of 80 °C in an oven and marked as $BC_{Mo/Mn700\text{-}2}$, $BC_{Mo/Mn800\text{-}1}$, $BC_{Mo/Mn800\text{-}2}$, $BC_{Mo/Mn800\text{-}3}$, and $BC_{Mo/Mn900\text{-}2}$. The numbers 1, 2, and 3 represent the increase of metal content in catalysts. Among them, the contents of Mo and Mn in $BC_{MoMn800\text{-}2}$ were detected by inductively coupled plasma optical emission spectrometry (ICP-OES) to be 6.53 and 8.61 wt%, respectively (Table S1†).

Characterization

Scanning electron microscopy (SEM, ZEISS GeminiSEM 300, Germany) and transmission electron microscopy (TEM, FEI Talos F200X, America) were used to record the microscopic morphology of the catalysts. X-ray Diffraction (XRD, Bruker D8 Advance, Germany) was used to analyze the crystal structure of the catalysts. A contact angle/surface tension meter (Lauda Scientific LSA100, Germany) was used to detect the hydrophilicity and hydrophobicity of the catalysts. The surface elemental composition and valence state of the catalysts were determined by X-ray photoelectron spectroscopy (XPS, Thermo Scientific K-Alpha, America). Raman spectroscopy (Raman, Horiba LabRAM HR Evolution, Japan) was used to analyze the degree of graphitization of catalysts. Metal elements including Mo and Mn were detected by inductively coupled plasma optical emission spectrometry (ICP-OES, Agilent 5110, America). The X-ray absorption fine structure spectra (XAFS) at the Mo/Mn K-edge of electrocatalysts were recorded at beamlines BL14W1 and BL11B in the Shanghai Synchrotron Radiation Facility (SSRF). Electrochemical measurements are provided in Text S1 of the ESI.†

Theoretical calculations

Spin-polarized DFT calculations were performed using the Vienna *ab initio* simulation package (VASP). The generalized gradient approximation proposed by Perdew, Burke, and Ernzerhof (GGA-PBE) was selected for the exchange–correlation potential. The pseudo-potential was described by the projector-augmented-wave (PAW) method. The geometry optimization was performed until the Hellmann–Feynman force on each atom was smaller than 0.02 eV $Å^{-1}$. The energy criterion was set to 10^{-6} eV in the iterative solution of the Kohn–Sham equation.

Data availability

The data that support the findings of this study are available from the corresponding authors upon reasonable request.

Author contributions

Chengyu Zhang: conceptualization, validation, methodology, investigation, writing-original draft. Xiangyang Wang, Renyuan Zhao: methodology, validation, investigation, writing-review & editing. Fabrice Ndayisenga: supervision, writing-review & editing. Zhisheng Yu: conceptualization, supervision, writing-review & editing, funding acquisition.

Conflicts of interest

The authors declare no competing financial interest.

Acknowledgements

This investigation was funded by the Binzhou Institute of Technology, (GYY-DTFZ-2022-003), the Fundamental Research

Funds for the Central Universities (E2E40503X2) and the Science and Technology Service Network Initiative Project of the Chinese Academy of Sciences (KFJ-STS-QYZX-112).

References

1 S. Chu and A. Majumdar, Opportunities and challenges for a sustainable energy future, *Nature*, 2012, **488**, 294–303.
2 Y. Sun, Z. Xue, Q. Liu, Y. Jia and G. Li, Modulating Electronic Structure of Metal-Organic Frameworks by Introducing Atomically Dispersed Ru for Efficient Hydrogen Evolution, *Nat. Commun.*, 2018, **8**, 1801564–1801570.
3 F. Podjaski, D. Weber, S. Zhang, L. Diehl and B. V. Lotsch, Rational Strain Engineering in Delafossite Oxides for Highly Efficient Hydrogen Evolution Catalysis in Acidic Media, *Nat. Catal.*, 2019, **3**, 55–63.
4 A. Odenweller, F. Ueckerdt, G. F. Nemet, M. Jensterle and G. Luderer, Probabilistic feasibility space of scaling up green hydrogen supply, *Nat. Energy*, 2022, **7**, 854–865.
5 J. Yu, Y. Guo, S. She, S. Miao, M. Ni, W. Zhou, M. Liu and Z. Shao, Bigger is surprisingly better: agglomerates of larger RuP nanoparticles outperform benchmark Pt nanocatalysts for the hydrogen evolution reaction, *Adv. Mater.*, 2018, **30**, 1800047–1800056.
6 Y. Bang, S. Park, S. J. Han, J. Yoo, J. H. Song, J. H. Choi, K. H. Kang and I. K. Song, Hydrogen production by steam reforming of liquefied natural gas (LNG) over mesoporous Ni/Al_2O_3 catalyst prepared by an EDTA-assisted impregnation method, *Appl. Catal., B*, 2016, **180**, 179–188.
7 F. Valentini, A. Marrocchi and L. Vaccaro, Liquid Organic Hydrogen Carriers (LOHCs) as H-Source for Bio-Derived Fuels and Additives Production, *Adv. Energy Mater.*, 2022, **12**, 2103362–2103390.
8 I. Roger, M. A. Shipman and M. D. Symes, Earth-abundant catalysts for electrochemical and photoelectrochemical water splitting, *Nat. Rev. Chem*, 2017, **1**, 0003–0016.
9 H. Sun, X. Xu, Y. Song, W. Zhou and Z. Shao, Designing high-valence metal sites for electrochemical water splitting, *Adv. Funct. Mater.*, 2021, **31**, 2009779–2009822.
10 B. Zhou, R. Gao, J. J. Zou and H. Yang, Surface design strategy of catalysts for water electrolysis, *Small*, 2022, **18**, 2202336–2202361.
11 W. Liu, X. Wang, F. Wang, K. Du, Z. Zhang, Y. Guo, H. Yin and D. Wang, A durable and pH-universal self-standing MoC–Mo_2C heterojunction electrode for efficient hydrogen evolution reaction, *Nat. Commun.*, 2021, **12**, 6776–6785.
12 K. Wang, S. Wang, K. S. Hui, H. Gao, D. A. Dinh, C. Yuan, C. Zha, Z. Shao, Z. Tang and K. N. Hui, Synergistically boosting the elementary reactions over multiheterogeneous ordered macroporous Mo_2C/NC-Ru for highly efficient alkaline hydrogen evolution, *Carbon Energy*, 2022, **4**, 856–866.
13 S. Nong, W. Dong, J. Yin, B. Dong, Y. Lu, X. Yuan, X. Wang, K. Bu, M. Chen, S. Jiang, L. M. Liu, M. Sui and F. Huang, Well-Dispersed Ruthenium in Mesoporous Crystal TiO_2 as an Advanced Electrocatalyst for Hydrogen Evolution Reaction, *J. Am. Chem. Soc.*, 2018, **140**(17), 5719–5727.
14 J. Chen, C. Chen, M. Qin, B. Li, B. Lin, Q. Mao, H. Yang, B. Liu and Y. Wang, Reversible hydrogen spillover in Ru-WO_{3-x} enhances hydrogen evolution activity in neutral pH water splitting, *Nat. Commun.*, 2022, **13**, 5382–5391.
15 L. Gong, J. Zhu, F. Xia, Y. Zhang, W. Shi, L. Chen, J. Yu, J. Wu and S. Mu, Marriage of Ultralow Platinum and Single-Atom MnN_4 Moiety for Augmented ORR and HER Catalysis, *ACS Catal.*, 2023, **13**, 4012–4020.
16 H. Liu, L. Jiang, J. Khan, X. Wang, J. Xiao, H. Zhang, H. Xie, L. Li, S. Wang and L. Han, Decorating Single-Atomic Mn Sites with FeMn Clusters to Boost Oxygen Reduction Reaction, *Angew. Chem., Int. Ed.*, 2023, **135**, 1–8.
17 F. Mo, C. Song, Q. Zhou, W. Xue, S. Ouyang, Q. Wang, Z. Hou, S. Wang and J. Wang, The optimized Fenton-like activity of Fe single-atom sites by Fe atomic clusters–mediated electronic configuration modulation, *Proc. Natl. Acad. Sci. U. S. A.*, 2023, **120**, 1–12.
18 Q. Wang, M. Ming, S. Niu, Y. Zhang, G. Fan and J. S. Hu, Scalable solid-state synthesis of highly dispersed uncapped metal (Rh, Ru, Ir) nanoparticles for efficient hydrogen evolution, *Adv. Energy Mater.*, 2018, **8**, 1801698–1801704.
19 D. H. Kweon, M. S. Okyay, S.-J. Kim, J.-P. Jeon, H.-J. Noh, N. Park, J. Mahmood and J.-B. Baek, Ruthenium anchored on carbon nanotube electrocatalyst for hydrogen production with enhanced Faradaic efficiency, *Nat. Commun.*, 2020, **11**, 1278–1287.
20 J. Wu, J. Su, T. Wu, L. Huang, Q. Li, Y. Luo, H. Jin, J. Zhou, T. Zhai and D. Wang, Scalable Synthesis of 2D Mo_2C and Thickness-Dependent Hydrogen Evolution on Its Basal Plane and Edges, *Adv. Mater.*, 2023, 2209954–2209961.
21 P. Li, G. Zhao, N. Cheng, L. Xia, X. Li, Y. Chen, M. Lao, Z. Cheng, Y. Zhao, X. Xu, Y. Jiang, H. Pan, S. X. Dou and W. Sun, Toward enhanced alkaline hydrogen electrocatalysis with transition metal-functionalized nitrogen-doped carbon supports, *Chin. J. Catal.*, 2022, **43**, 1351–1359.
22 J. Yang, B. Chen, X. Liu, W. Liu, Z. Li, J. Dong, W. Chen, W. Yan, T. Yao, X. Duan, Y. Wu and Y. Li, Efficient and Robust Hydrogen Evolution: Phosphorus Nitride Imide Nanotubes as Supports for Anchoring Single Ruthenium Sites, *Angew. Chem., Int. Ed.*, 2018, **57**, 9495–9500.
23 Q. Hu, K. Gao, X. Wang, H. Zheng, J. Cao, L. Mi, Q. Huo, H. Yang, J. Liu and C. He, Subnanometric Ru clusters with upshifted D band center improve performance for alkaline hydrogen evolution reaction, *Nat. Commun.*, 2022, **13**, 3958–3967.
24 Y. Gong, D. Li, C. Luo, Q. Fu and C. Pan, Highly porous graphitic biomass carbon as advanced electrode materials for supercapacitors, *Green Chem.*, 2017, **19**, 4132–4140.
25 P. Aggarwal, D. Sarkar, K. Awasthi and P. W. Menezes, Functional role of single-atom catalysts in electrocatalytic hydrogen evolution: current developments and future challenges, *Coord. Chem. Rev.*, 2022, **452**, 214289–214323.
26 J. Ji, Y. Zhang, L. Tang, C. Liu, X. Gao, M. Sun, J. Zheng, M. Ling, C. Liang and Z. Lin, Platinum single-atom and cluster anchored on functionalized MWCNTs with

ultrahigh mass efficiency for electrocatalytic hydrogen evolution, *Nano Energy*, 2019, **63**, 103849–103856.

27 N. Cheng, S. Stambula, D. Wang, M. N. Banis, J. Liu, A. Riese, B. Xiao, R. Li, T.-K. Sham and L.-M. Liu, Platinum single-atom and cluster catalysis of the hydrogen evolution reaction, *Nat. Commun.*, 2016, **7**, 13638–13647.

28 S. Sultan, J. N. Tiwari, A. N. Singh, S. Zhumagali, M. Ha, C. W. Myung, P. Thangavel and K. S. Kim, Single atoms and clusters based nanomaterials for hydrogen evolution, oxygen evolution reactions, and full water splitting, *Adv. Energy Mater.*, 2019, **9**, 1900624–1900671.

29 L. Zhang, J. Zhu, X. Li, S. Mu, F. Verpoort, J. Xue, Z. Kou and J. Wang, Nurturing the marriages of single atoms with atomic clusters and nanoparticles for better heterogeneous electrocatalysis, *Interdiscipl. Mater.*, 2022, **1**, 51–87.

30 G. Humagain, K. MacDougal, J. MacInnis, J. M. Lowe, R. H. Coridan, S. MacQuarrie and M. Dasog, Highly Efficient, Biochar-Derived Molybdenum Carbide Hydrogen Evolution Electrocatalyst, *Adv. Energy Mater.*, 2018, **8**, 1801461–1801465.

31 J.-S. Li, Y. Wang, C.-H. Liu, S.-L. Li, Y.-G. Wang, L.-Z. Dong, Z.-H. Dai, Y.-F. Li and Y.-Q. Lan, Coupled molybdenum carbide and reduced graphene oxide electrocatalysts for efficient hydrogen evolution, *Nat. Commun.*, 2016, **7**, 11204–11211.

32 X. Zhou, Z. Yu, Y. Yao, Y. Jiang, X. Rui, J. Liu and Y. Yu, A High-Efficiency Mo2C Electrocatalyst Promoting the Polysulfide Redox Kinetics for Na–S Batteries, *Adv. Mater.*, 2022, **34**, 2200479–2200487.

33 D. J. Sprouster, W. Streit Cunningham, G. P. Halada, H. Yan, A. Pattammattel, X. Huang, D. Olds, M. Tilton, Y. S. Chu, E. Dooryhee, G. P. Manogharan and J. R. Trelewicz, Dislocation microstructure and its influence on corrosion behavior in laser additively manufactured 316L stainless steel, *Addit. Manuf.*, 2021, **47**, 102263–102275.

34 J. Kang, L. Zhou, X. Duan, H. Sun, Z. Ao and S. Wang, Degradation of Cosmetic Microplastics via Functionalized Carbon Nanosprings, *Matter*, 2019, **1**, 745–758.

35 S. Amelinckx, X. B. Zhang, D. Bernaerts, X. F. Zhang, V. Ivanov and J. B. Nagy, A formation mechanism for catalytically grown helix-shaped graphite nanotubes, *Science*, 1994, **265**, 635–639.

36 M. Liu and J. M. Cowley, Encapsulation of manganese carbides within carbon nanotubes and nanoparticles, *Carbon*, 1995, **33**, 749–756.

37 Y. Wang, Y. Wang, X. Wang, M. Chang, G. Zhang, X. Mao, Y. Li, J. Wang and L. Wang, Efficient activation of peroxodisulfate by novel bionic iron-encapsulated biochar: the key roles of electron transfer pathway and reactive oxygen species evolution, *J. Hazard. Mater.*, 2023, **443**, 130204–130214.

38 Z. Yang, X. Yang, G. An and D. Wang, Regulating spin state of Fe active sites by the P-doping strategy for enhancing peroxymonosulfate activation, *Appl. Catal. B Environ.*, 2023, **330**, 122618–122627.

39 G. Yang, J. Zhu, P. Yuan, Y. Hu, G. Qu, B.-A. Lu, X. Xue, H. Yin, W. Cheng, J. Cheng, W. Xu, J. Li, J. Hu, S. Mu and J.-N. Zhang, Regulating Fe-spin state by atomically dispersed Mn-N in Fe-N-C catalysts with high oxygen reduction activity, *Nat. Commun.*, 2021, **12**, 1734–1743.

40 X. Cui, L. Gao, S. Lei, S. Liang, J. Zhang, C. D. Sewell, W. Xue, Q. Liu, Z. Lin and Y. Yang, Simultaneously crafting single-atomic Fe sites and graphitic layer-wrapped Fe_3C nanoparticles encapsulated within mesoporous carbon tubes for oxygen reduction, *Adv. Funct. Mater.*, 2021, **31**, 2009197–2009205.

41 Y. Wang, P. Lv, J. Pan, J. Chen, X. Liu, M. Hu, L. Wan, K. Cao, B. Liu and Z. Ku, Grain Boundary Elimination via Recrystallization-Assisted Vapor Deposition for Efficient and Stable Perovskite Solar Cells and Modules, *Adv. Mater.*, 2023, **35**, 2304625–2304632.

42 X. Wu, Z. Wang, D. Zhang, Y. Qin, M. Wang, Y. Han, T. Zhan, B. Yang, S. Li and J. Lai, Solvent-free microwave synthesis of ultra-small Ru-Mo_2C@CNT with strong metal-support interaction for industrial hydrogen evolution, *Nat. Commun.*, 2021, **12**, 4018–4027.

43 Z. Yang, X. Wang, M. Zhu, X. Leng, W. Chen, W. Wang, Q. Xu, L.-M. Yang and Y. Wu, Structural revolution of atomically dispersed Mn sites dictates oxygen reduction performance, *Nano Res.*, 2021, **14**, 4512–4519.

44 X. Xie, L. Peng, H. Yang, G. I. N. Waterhouse, L. Shang and T. Zhang, MIL-101-derived mesoporous carbon supporting highly exposed Fe single-atom sites as efficient oxygen reduction reaction catalysts, *Adv. Mater.*, 2021, **33**, 2101038–2101045.

45 J. Feng, H. Gao, L. Zheng, Z. Chen, S. Zeng, C. Jiang, H. Dong, L. Liu, S. Zhang and X. Zhang, A Mn-N_3 single-atom catalyst embedded in graphitic carbon nitride for efficient CO_2 electroreduction, *Nat. Commun.*, 2020, **11**, 4341–4348.

46 D. Guo, R. Shibuya, C. Akiba, S. Saji, T. Kondo and J. Nakamura, Active sites of nitrogen-doped carbon materials for oxygen reduction reaction clarified using model catalysts, *Science*, 2016, **351**, 361–365.

47 Z. Chen, X. Liao, C. Sun, K. Zhao, D. Ye, J. Li, G. Wu, J. Fang, H. Zhao and J. Zhang, Enhanced performance of atomically dispersed dual-site Fe-Mn electrocatalysts through cascade reaction mechanism, *Appl. Catal. B Environ.*, 2021, **288**, 120021–120028.

48 L. He, W. Zhang, Q. Mo, W. Huang, L. Yang and Q. Gao, Molybdenum Carbide-Oxide Heterostructures: In Situ Surface Reconfiguration toward Efficient Electrocatalytic Hydrogen Evolution, *Angew. Chem., Int. Ed.*, 2020, **59**, 3544–3548.

49 J. Staszak-Jirkovský, C. D. Malliakas, P. P. Lopes, N. Danilovic, S. S. Kota, K.-C. Chang, B. Genorio, D. Strmcnik, V. R. Stamenkovic, M. G. Kanatzidis and N. M. Markovic, Design of active and stable Co–Mo–S_x chalcogels as pH-universal catalysts for the hydrogen evolution reaction, *Nat. Mater.*, 2016, **15**, 197–203.

50 J. Zhang, T. Wang, P. Liu, Z. Liao, S. Liu, X. Zhuang, M. Chen, E. Zschech and X. Feng, Efficient hydrogen production on $MoNi_4$ electrocatalysts with fast water dissociation kinetics, *Nat. Commun.*, 2017, **8**, 15437–15444.

51 H. Shang, Z. Jiang, D. Zhou, J. Pei, Y. Wang, J. Dong, X. Zheng, J. Zhang and W. Chen, Engineering a metal-organic framework derived Mn-N_4-C_xS_y atomic interface for highly efficient oxygen reduction reaction, *Chem. Sci.*, 2020, **11**, 5994–5999.

52 C. Zhu, A. L. Wang, W. Xiao, D. Chao, X. Zhang, N. H. Tiep, S. Chen, J. Kang, X. Wang and J. Ding, In situ grown epitaxial heterojunction exhibits high-performance electrocatalytic water splitting, *Adv. Mater.*, 2018, **30**, 1705516–1705523.

53 X. Ye, J. Ma, W. Yu, X. Pan, C. Yang, C. Wang, Q. Liu and Y. Huang, Construction of bifunctional single-atom catalysts on the optimized β-Mo_2C surface for highly selective hydrogenation of CO_2 into ethanol, *J. Energy Chem.*, 2021, **67**, 184–192.

54 D. V. Lam, U. N. T. Nguyen, E. Roh, W. Choi, J. H. Kim, H. Kim and S. M. Lee, Graphitic Carbon with MnO/Mn_7C_3 Prepared by Laser-Scribing of MOF for Versatile Supercapacitor Electrodes, *Small*, 2021, **17**, 2100670–2100678.

55 X. Han, T. Zhang, W. Chen, B. Dong, G. Meng, L. Zheng, C. Yang, X. Sun, Z. Zhuang and D. Wang, Mn-N_4 Oxygen Reduction Electrocatalyst: Operando Investigation of Active Sites and High Performance in Zinc–Air Battery, *Adv. Energy Mater.*, 2021, **11**, 2002753–2002761.

56 P. Cui, C. Liu, X. Su, Q. Yang, L. Ge, M. Huang, F. Dang, T. Wu and Y. Wang, Atomically Dispersed Manganese on Biochar Derived from a Hyperaccumulator for Photocatalysis in Organic Pollution Remediation, *Environ. Sci. Technol.*, 2022, **56**, 8034–8042.

57 Y. Li, J. Li, J. Chen, P. Cai, G. Wang, Y. Hou, L. Lei and Z. Wen, RuS2-x quantum dots/rGO as bifunctional hydrogen electrocatalysts for harvesting electrochemical neutralization energy, *J. Power Sources*, 2020, **472**, 228625–228631.

58 L. Li, P. Wang, Q. Shao and X. Huang, Metallic nanostructures with low dimensionality for electrochemical water splitting, *Chem. Soc. Rev.*, 2020, **49**, 3072–3106.

59 M. Wang, X. Yu, Z. Wang, X. Gong, Z. Guo and L. Dai, Hierarchically 3D porous films electrochemically constructed on gas–liquid–solid three-phase interface for energy application, *J. Mater. Chem.*, 2017, **5**, 9488–9513.

60 A. K. Kota, Y. Li, J. M. Mabry and A. Tuteja, Hierarchically Structured Superoleophobic Surfaces with Ultralow Contact Angle Hysteresis, *Adv. Mater.*, 2012, **24**, 5838–5843.

61 X. Yu, M. Wang, Z. Wang, X. Gong and Z. Guo, 3D multi-structural porous NiAg films with nanoarchitecture walls: high catalytic activity and stability for hydrogen evolution reaction, *Electrochim. Acta*, 2016, **211**, 900–910.

62 R. Li and D. Wang, Superiority of dual-atom catalysts in electrocatalysis: one step further than single-atom catalysts, *Adv. Energy Mater.*, 2022, **12**, 2103564–2103596.

63 J. Mahmood, F. Li, S.-M. Jung, M. S. Okyay, I. Ahmad, S.-J. Kim, N. Park, H. Y. Jeong and J.-B. Baek, An efficient and pH-universal ruthenium-based catalyst for the hydrogen evolution reaction, *Nat. Nanotechnol.*, 2017, **12**, 441–446.

64 P. Zhou, L. Tao, S. Tao, Y. Li, D. Wang, X. Dong, T. Frauenheim, X. Fu, X. Lv and S. Wang, Construction of nickel-based dual heterointerfaces towards accelerated alkaline hydrogen evolution via boosting multi-step elementary reaction, *Adv. Funct. Mater.*, 2021, **31**, 2104827–2104836.